Cryogenics 73 (2016) 53–59

Contents lists available at ScienceDirect

Cryogenics

journal homepage: www.elsevier.com/locate/cryogenics

CFD simulation of a miniature coaxial Stirling-type pulse tube cryocooler operating at 128 Hz

Yibo Zhao [a,b], Haizheng Dang [a,*]

[a] National Laboratory for Infrared Physics, Shanghai Institute of Technical Physics, Chinese Academy of Sciences, 500 Yutian Road, Shanghai 200083, China
[b] University of Chinese Academy of Sciences, No. 19A Yuquan Road, Beijing 100049, China

ARTICLE INFO

Article history:
Received 8 September 2015
Received in revised form 11 November 2015
Accepted 23 November 2015
Available online 2 December 2015

Keywords:
CFD simulations
Miniature
Coaxial
Stirling-type pulse tube cryocooler
128 Hz

ABSTRACT

A two-dimensional axis-symmetric CFD model of a miniature coaxial Stirling-type pulse tube cryocooler with an overall weight of 920 g operating at 128 Hz is established, and systematic simulations of the performance characteristics at different temperatures are conducted. Both thermal equilibrium and non-equilibrium mechanisms for the porous matrix are considered, and the regenerator losses including the gas and solid conduction, the pressure drop and the imperfect interfacial heat transfer are calculated, respectively. The results indicate that the pressure drop loss is dominant during the first 85% and 78% of regenerator length for the thermal equilibrium and non-equilibrium models, respectively, and it decreases monotonously from warm to cold end due to the steadily decreasing Darcy and Forchheimer terms, whereas other entropy generations share similar changing tendencies, going up gradually near the warm end, increasing dramatically from about 60% of length and then decreasing sharply near the cold end. The reasons for these entropy variations are discussed.

1. Introduction

The recent years have witnessed the rapid development and miniaturization of low-temperature sensors. Many of the sensors are optical and electronic based technologies, which actually require only a relatively small heat lift, such as 1–2 W or even less, but normally, they do need short cooldown times. Traditionally, a certain recuperative cryocooler, namely, the open-loop JT cryocooler, is the main force used for the needed short cooldown time. One of the main reasons for the choice is that there is no any moving part at the cold end of the JT cryocooler, and thus the cold head can be miniaturized easily. The miniaturization, together with a considerably high pressure, such as 20–50 MPa, results in a very rapid cool-down, typically a few seconds to reach 77 K, thereby making the open-loop JT cryocooler a relatively ideal choice for cooling infrared sensors used in missile guidance. The main disadvantages of the open-loop JT cryocooler include the very high charging pressure, the susceptibility to plugging of the orifice in the valve, the low cooling efficiency, and especially, a very short cooling duration. For example, in the open-cycle mode, cooling lasts for only a few minutes until the gas is depleted. Most applications, either in space or on ground, actually require a much longer cooling duration, and thus an alternative, namely, the miniature closed-loop JT cryocooler is suggested. Unfortunately, the great difficulties in design and optimization have severely hampered the development of the practical closed-loop JT cryocooler. Therefore, there has been a growing interest in miniaturizing regenerative cryocoolers, especially the Stirling-type pulse tube cryocooler (SPTC). The charging pressure in the regenerative cryocooler is much lower, typically only in the range of 1–5 MPa, however, the cooling efficiency is generally much higher than that of the open-loop JT. Especially for those regenerative cryocoolers employing linear compressors, such as Stirling cryocooler and SPTC, the relative Carnot efficiencies at 80 K could be generally more than five times that of the open-loop JT. The SPTC is also well known for its long life, for example, an excellent space SPTC could continuously operate for over 10 years. Another important reason for the strong interest in miniaturizing the SPTC is that, similar to JT, there is no moving part at the cold end either, thereby also greatly facilitating the miniaturization.

Besides the attractive merit of rapid cool-down, when used in space, the miniature cryocooler can bring the benefit of low mass, small volume and resultant low cost. A miniature space SPTC with high reliability and high cooling capacity is desirable for some small infrared focal planes, filters or cold optics that currently use heavier cold radiators.

* Corresponding author. Tel.: +86 21 25051967; fax: +86 21 65830734.
E-mail address: haizheng.dang@mail.sitp.ac.cn (H. Dang).

http://dx.doi.org/10.1016/j.cryogenics.2015.11.007
0011-2275/

Nomenclature

A_{reg}	cross-sectional area of regenerator (m^2)
A_{fs}	interfacial area density (m^{-1})
C_2	inertial resistance factor (m^{-1})
C_p	heat capacity (J/kg K)
d_h	hydraulic diameter (m)
d_w	wire diameter (m)
E	specific energy (J/kg)
f	operating frequency (Hz)
f_{osc}	friction factor
h	specific enthalpy (J/kg)
h_{fs}	heat transfer coefficient (W/m^2 K)
k	thermal conductivity (W/m K)
k_{eff}	effective thermal conductivity (W/m K)
m	mesh number
Nu	Nusselt number
p	pressure (Pa)
p_0	charging pressure (Pa)
Δp	amplitude of the dynamic pressure (Pa)
Pr	Prandtl number
$\dot{Q}_c$	cooling capacity (W)
Re	Reynolds number
S_i	moment source term (N/m^3)
$\dot{S}_{gen,f}$	entropy generation for gas conduction (W/K)
$\dot{S}_{gen,s}$	entropy generation for solid conduction (W/K)
$\dot{S}_{gen,p}$	entropy generation for pressure drop (W/K)
$\dot{S}_{gen,fs}$	entropy generation for interface heat transfer (W/K)
T	temperature (K)
v	velocity (m/s)
$\langle \dot{W}_{pv} \rangle$	time-averaged input PV power (W)
Δx	node distance (m)

Greek symbols

α	permeability (m^2)
ε	porosity
μ	viscosity (Pa s)
ρ	density (kg/m^3)
$\bar{\bar{\tau}}$	stress tensor (N/m^2)
φ	phase angle (rad)

Subscripts

f	fluid
s	solid matrix
h	warm end
c	cold end
i	node i
$i+1$	node $i+1$
avg	cycle averaged

For the regenerative cryocooler, the cooling capacity decreases sharply with the reducing size. The guiding principle of solving the problem is to increase the charging pressure and the cycle frequency to compensate for the decrease in working fluid volume. Peterson and Al Hazmy [1] studied the size limits for Stirling cycle refrigerators, and Shire et al. [2] also conducted investigations of microscale cryocoolers. The above studies tried to establish a theoretical lower size limit to the regenerative cryocooler miniaturization. Radebaugh and O'Gallagher [3] investigated the heat transfer in small dimensions and at higher frequency operation, and tried to establish the necessary operating parameters and regenerator geometries necessary to design viable high frequency miniature cryocoolers.

Some impressive progress has also been made in the experimental development of miniaturizing the SPTC. For example, Petach et al. [4] designed a 782 g miniature coaxial SPTC prototype for space applications, which could lift 1.1 W at 77 K with an input power of 50 W operating at about 100 Hz, which was further developed into an Engineering Model version [5,6], weighting 857 g, and achieved a cooling capacity of 1.3 W at 77 K with an expected lifetime of more than 10 years. Olson et al. [7] developed a very lightweight SPTC, with the micro compressor and the cold finger weighting 190 g and 120 g, respectively, which achieved a cooling capacity of 650 mW at 150 K with an electrical power of 10 W at around 100 Hz, having the potential for both tactical and space applications. Vanapalli et al. [8] ever designed a miniature SPTC cold finger operating at 120 Hz and Radebaugh et al. [9] did another resonating at 150 Hz by employing commercial miniature linear compressors, and Lopes et al. [10] also developed a 100 Hz miniature SPTC cold finger prototype. But please note that in the last three cases, either the miniaturization of the linear compressors was not realized [8,10], or the mismatch of the compressor and the cold finger happened [9].

As discussed in the above survey, although some theoretical and experimental investigations have been conducted on the miniaturization of the SPTC, systematic studies about the physical mechanism and flow characteristics inside the miniature system, especially in a coaxial miniature system at such high frequencies, are seldom made. Since the CFD method based on two- or three-dimensional models is an effective approach to detailed analyses of the internal process in a SPTC, we will establish a two-dimensional axis-symmetric CFD model of a miniature coaxial SPTC operating at 128 Hz, with the moving-coil linear compressor and pulse tube cold finger weighting about 650 g and 270 g, respectively. Based on the model, the regenerator losses and the cooler performance characteristics will be analyzed and summarized. Both thermal equilibrium and non-equilibrium models for the porous matrix will be considered.

2. CFD simulation model

2.1. CFD simulation approaches for the PTC

The one-dimensional (1-D) model [11] was widely used for the analysis and optimization of the PTC. In recent years, in order to achieve more accurate and detailed description of the flow and heat transfer processes, several 2-D models have been suggested. For example, Flake and Razani [12] presented 2-D axis-symmetric models of a basic and an orifice PTC using Fluent® and demonstrated circulation patterns near the heat exchangers (HXs) and a steady streaming effect in the pulse tube. Cha et al. [13] simulated two inertance tube PTCs using a CFD code and showed that significant multi-dimensional effects and secondary-flow recirculation occurred when components had relatively small L/D ratios. Ashwin et al. [14] modeled an inertance type PTC with thermal equilibrium and non-equilibrium conditions of porous zones, in which the effect of finite wall thickness of the components was taken into account.

The abovementioned CFD models were primarily focused on the mid-sized SPTCs with the in-line arrangement, and the operating frequencies are mainly below 60 Hz, while the miniature SPTC with the coaxial arrangement operating at very high frequencies are seldom conducted. In this paper, a 2-D axis-symmetric CFD model of a miniature coaxial SPTC with the overall mass of about 920 g operating at 128 Hz will be established with the aid of

Fluent® package [15], and the systematic simulations of the performance characteristics of it will be presented.

2.2. Model building

Fig. 1 shows a schematic of the miniature PTC with its main components, and Fig. 2 shows its 2-D axis-symmetric geometry, which consists of an aftercooler, a regenerator, a cold heat exchanger (CHX), a pulse tube, a warm heat exchanger (WHX), two inertance tubes with different diameters and lengths, and a reservoir. The shaded parts represent porous zones. Table 1 gives the geometric dimensions and boundary conditions of these components. The geometries of the cold finger and operating parameters have been optimized initially by the one-dimensional numerical simulation method developed in the same laboratory [16,17].

In the simulation of the cold finger, the micro compressor is replaced by a pressure inlet at the left side of the aftercooler. The operating frequency f and the charging pressure p_0 are set at 128 Hz and 3.6 MPa, respectively. A User Defined Function (UDF) is used to define the inlet pressure which is given by:

$$p_{in} = p_0 + \Delta p \sin 2\pi f t \tag{1}$$

where the amplitude of the dynamic pressure Δp is valued to be 0.377 MPa. The pressure ratio at the inlet of the WHX is 1.23, which is obtained from the previous 1-D simulation results [16,17].

The working fluid of helium is regarded as an ideal gas, and its thermal properties, such as the thermal conductivity and viscosity, are temperature-dependent. Based on the previous empirical data and simulation results, the Reynolds number of the fluid in the cold finger does not reach the critical value, and thus the laminar flow model is employed.

2.3. Governing equations

The governing equations for the 2-D axis-symmetric model include mass, momentum and energy conservation equations [15]. For the gas domain, the conservation equations are given by:

$$\frac{\partial \rho_f}{\partial t} + \nabla \cdot (\rho_f \vec{v}) = 0 \tag{2}$$

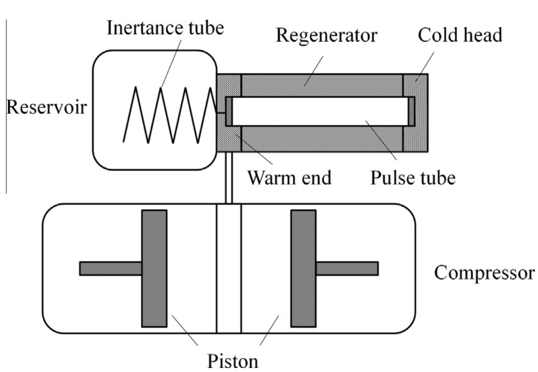

Fig. 1. Schematic of a miniature coaxial SPTC.

Table 1
Geometrical dimensions and boundary conditions.

Component	Radius (mm)	Length (mm)	Boundary condition
Aftercooler	6.5	5	T_w = 300 K
Regenerator	6.5	24	Adiabatic
CHX	6.5	5	Adiabatic
Pulse tube	2.5	30	Adiabatic
WHX	2.5	2	T_w = 300 K
Inertance tube 1	0.85	560	T_w = 300 K
Inertance tube 2	1.05	720	T_w = 300 K
Reservoir	15	40	T_w = 300 K

$$\frac{\partial}{\partial t}(\rho_f \vec{v}) + \nabla \cdot (\rho_f \vec{v}\vec{v}) = -\nabla p + \nabla \cdot (\bar{\bar{\tau}}) \tag{3}$$

$$\frac{\partial}{\partial t}(\rho_f E_f) + \nabla \cdot [\vec{v}(\rho_f E_f + p)] = \nabla \cdot [k_f \nabla T + (\bar{\bar{\tau}} \cdot \vec{v})] \tag{4}$$

where ρ_f, $\vec{v}$, p, T, k_f and E_f are the density, velocity, static pressure, temperature, thermal conductivity and total energy of the fluid, respectively. $\bar{\bar{\tau}}$ is the stress tensor.

However, for porous zones, the properties of the solid matrix should be taken into account. Thus, the mass and momentum conservation equations are rewritten as:

$$\frac{\partial(\varepsilon \rho_f)}{\partial t} + \nabla \cdot (\varepsilon \rho_f \vec{v}) = 0 \tag{5}$$

$$\frac{\partial}{\partial t}(\varepsilon \rho_f \vec{v}) + \nabla \cdot (\varepsilon \rho_f \vec{v}\vec{v}) = -\varepsilon \nabla p + \nabla \cdot (\varepsilon \bar{\bar{\tau}}) + S_i \tag{6}$$

where ε is the porosity of the medium, S_i is the source term for the momentum equation, which is composed of two parts: the Darcy term and the Forchheimer term [15]:

$$S_i = -\left(\frac{\mu}{\alpha}\vec{v} + \frac{C_2}{2}\rho_f |\vec{v}|\vec{v}\right) \tag{7}$$

where α is the permeability and C_2 is the inertial resistance factor.

The energy conservation equation based on the thermal equilibrium mode is given by:

$$\frac{\partial}{\partial t}[\varepsilon \rho_f E_f + (1-\varepsilon)\rho_s E_s] + \nabla \cdot [\vec{v}(\rho_f E_f + p)] = \nabla \cdot [k_{eff} \nabla T + (\bar{\bar{\tau}} \cdot \vec{v})] \tag{8}$$

where k_{eff} is the effective thermal conductivity in the porous medium, ρ_s and E_s are the density and total energy of the solid, respectively. The thermal equilibrium mode assumes that there is no temperature difference between the fluid and the solid matrix in the porous zone, and thus the imperfect heat transfer loss between them is ignored and the effectiveness is assumed = 1.

In order to achieve more accurate results, the thermal non-equilibrium mode is also considered, in which the temperature difference between the fluid and the solid matrix is taken into account, and the energy conservation equations for the fluid and the solid matrix should be solved separately. For the fluid zone, it can be written as:

$$\frac{\partial}{\partial t}(\varepsilon \rho_f E_f) + \nabla \cdot [\vec{v}(\rho_f E_f + p)] = \nabla \cdot [\varepsilon k_f \nabla T_f + (\bar{\bar{\tau}} \cdot \vec{v})] + h_{fs} A_{fs}(T_s - T_f) \tag{9}$$

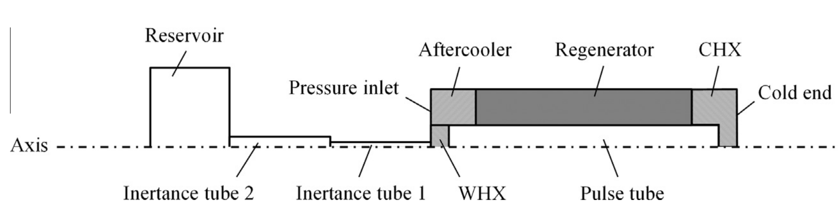

Fig. 2. 2-D axis-symmetric CFD model of the miniature coaxial SPTC.

For the solid zone, the energy conservation equation can be written as:

$$\frac{\partial}{\partial t}[(1-\varepsilon)\rho_s E_s] = \nabla \cdot [(1-\varepsilon)k_s \nabla T_s + (\bar{\bar{\tau}} \cdot \vec{v})] + h_{fs}A_{fs}(T_f - T_s) \quad (10)$$

where k_s represents the thermal conductivity for the solid material. h_{fs} is the heat transfer coefficient for the interface and A_{fs} is the interfacial area density. T_f and T_s are static temperatures of the fluid and the solid matrix, respectively.

2.4. Parameters setting

The porous zones consist of stacked mesh screens. The porosity can be calculated by [18]:

$$\varepsilon = 1 - \frac{\pi m d_w}{4 \times 0.0254} \quad (11)$$

where m is the mesh number and d_w is the wire diameter. The hydraulic diameter is given by:

$$d_h = \frac{\varepsilon}{1-\varepsilon} d_w \quad (12)$$

The interfacial area density is:

$$A_{fs} = \frac{4(1-\varepsilon)}{d_w} \quad (13)$$

The pressure drop through the porous zone in axial direction can be expressed as:

$$\frac{dp}{dx} = -\frac{f_{osc}}{2d_h}\rho_f v^2 \quad (14)$$

where f_{osc} is the screen friction factor under the oscillating flow conditions, which is a variation of the Ergun equation [19]:

$$f_{osc} = \frac{129}{Re} + 2.91Re^{-0.103} \quad (15)$$

where Re is the Reynolds number of the fluid in porous zones.

Based on Eqs. (7), (14) and (15), the permeability and inertial resistance factor are determined by the following equations:

$$\alpha = \frac{d_h^2}{64.5} \quad (16)$$

$$C_2 = \frac{2.91}{d_h} Re^{-0.103} \quad (17)$$

For the woven screen, k_{eff} can be obtained by [20]:

$$k_{eff} = k_f\varepsilon + k_s(1-\varepsilon)\left(\frac{k_s}{k_f}\right)^{-0.835}\left[\frac{3\left(\frac{k_s}{k_f}-\varepsilon\right) + \left(2+\frac{k_s}{k_f}\right)\varepsilon}{3(1-\varepsilon) + \left(2+\frac{k_s}{k_f}\right)\varepsilon}\right] \quad (18)$$

The heat transfer coefficient h_{fs} for the interface between fluid and solid matrix is:

$$h_{fs} = \frac{Nu \cdot k_f}{d_h} \quad (19)$$

where the Nusselt number Nu is given by [21]:

$$Nu = [1 + 0.99(Re \cdot Pr)^{0.66}]\varepsilon^{1.79} \quad (20)$$

where Pr is the Prandtl number. All of fluid and solid thermal properties are temperature-dependent and then expressed by mean values through porous zones.

Table 2 provides the parameters of mesh screens used in porous zones. Table 3 gives the different cases considered in the models, in which Case 1 is used as the basis of optimization.

Table 3
Parameters in different cases.

Case number	Operating frequency (Hz)	Porous zones	Cold end
1	128	Thermal equilibrium	Adiabatic
2	128	Thermal equilibrium	T_c = 80 K
3	128	Thermal equilibrium	T_c = 100 K
4	128	Thermal equilibrium	T_c = 150 K
5	128	Thermal non-equilibrium	Adiabatic

2.5. Solution approaches

This CFD model uses a first order implicit unsteady pressure based segregated solver with PISO pressure–velocity coupling. The pressure discretization employs the standard method while the second order upwinding is used for density, momentum and energy terms. The convergence criterion is 10^{-3} for continuity and velocity and 10^{-6} for energy. A time step of 5×10^{-5} s and 50 maximum iterations per time step are set for cases. The number of grid nodes is up to 6285 and no noticeable difference about the cooling performance is observed when this number is increased to 18,237.

3. Results and discussions

3.1. Thermal equilibrium model

As shown in Table 3, Case 1 represents the no-load condition and Cases 2–4 are used for predicting the cooling capacity with cold end temperatures of 80 K, 100 K and 150 K, respectively. The above four cases are based on the thermal equilibrium mode for porous zones and all operate at 128 Hz.

Fig. 3 shows the cool-down curve for Case 1. The lowest cycle-averaged no-load temperature of 64.5 K is achieved from an initial temperature of 300 K after about 100 s, about 9.5 K higher than the 1-D simulation result of 55 K. This difference is primarily caused by the additional loss due to multi-dimensional flow effects considered in the 2-D simulation, which is closer to the actual conditions.

Table 4 summarizes the cooling performance for Cases 2–4, when T_c is 80 K, 100 K and 150 K, respectively. A cooling capacity of 1.25 W at 80 K can be achieved with an input PV power of 49.3 W. It also shows that the input PV power increases when the cold end temperature decreases, which indicates that the lower cold end temperature leads to the lower impedance along the cold finger.

Fig. 4 compares the cooling capacities from 60 K to 100 K simulated by the 2-D CFD model with those by the previous 1-D numerical simulation, which indicates that there exists a difference of

Table 2
Parameters of mesh screens.

Components	Material	m	d_w (μm)	ε	d_h (μm)	α (m^2)	C_2 (m^{-1})	h_{fs} (W/m^2 K)	A_{fs} (m^{-1})
Regenerator	SS304	635	20	0.607	31.4	1.5×10^{-11}	81,460	15,813	77,448
Aftercooler	Copper	100	100	0.691	222.6	7.7×10^{-10}	12,173	8604	12,360
CHX	Copper	100	100	0.691	222.6	7.7×10^{-10}	12,173	19,464	12,360
WHX	Copper	100	100	0.691	222.6	7.7×10^{-10}	12,173	11,714	12,360

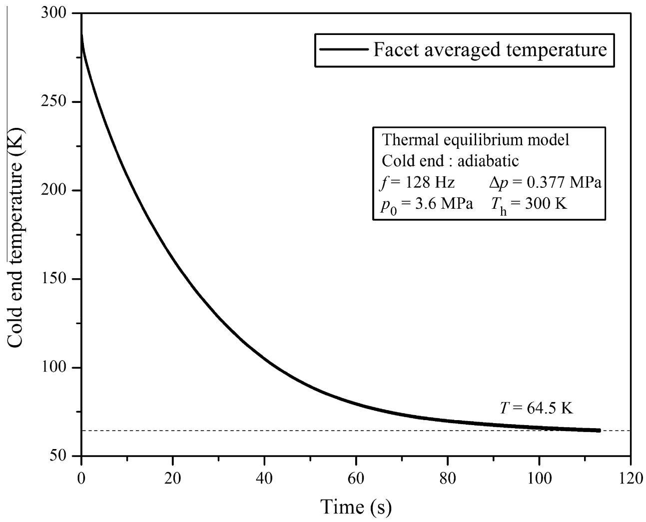

Fig. 3. Cool-down curve for Case 1.

Table 4
Cooling performance in Cases 2–4.

Case number	T_c (K)	$\dot{Q}_c$ (W)	$\langle \dot{W}_{pv} \rangle$ (W)
2	80	1.25	49.3
3	100	2.35	44.1
4	150	3.76	35.6

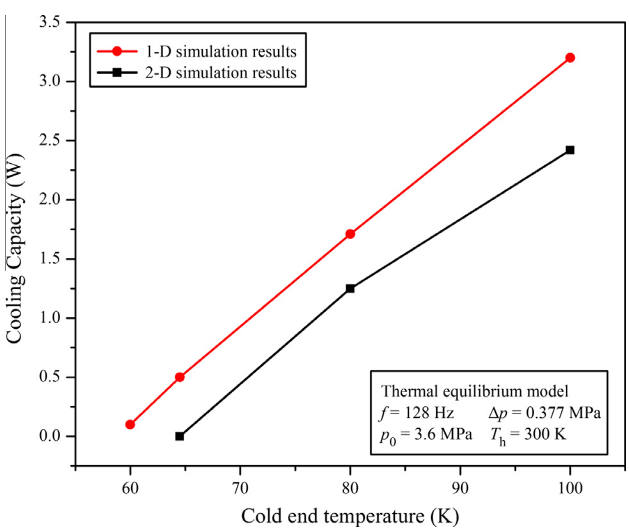

Fig. 4. Comparison of cooling capacities between 2-D and 1-D models.

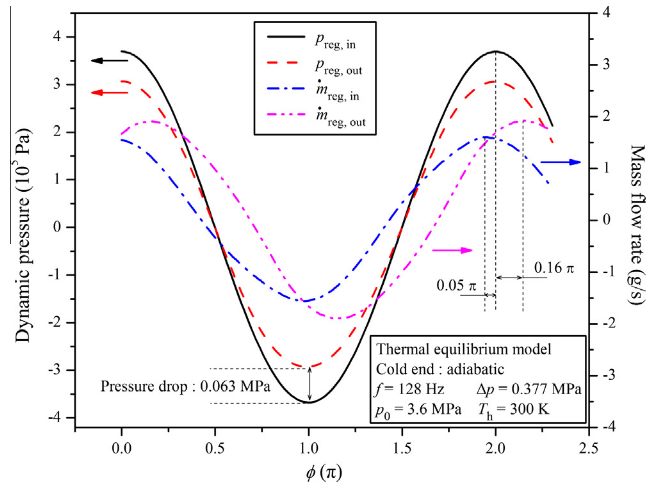

Fig. 5. Variations of the dynamic pressure and the mass flow rate at the inlet and outlet of the regenerator for Case 1.

about 0.5 W for each case, with the values in the 2-D CFD model always smaller. As discussed above, the multi-dimensional flow effects are primarily responsible for the additional loss.

Fig. 5 shows the temporal variations of the dynamic pressure and the mass flow rates at the inlet and outlet of the regenerator in Case 1. The pressure drop along the whole regenerator is about 0.063 MPa, and the phase shift of the pressure wave from warm to cold end is below 0.01π, which is very slight and can be ignored. The phase of the mass flow rate leads that of the pressure wave about 0.05π at the inlet, but lags 0.16π at the outlet. Therefore, the impedance in the regenerator causes a phase shift of nearly 0.21π for the mass flow rate.

The regenerator losses are mainly caused by gas conduction, solid conduction, the pressure drop, and the imperfect interfacial heat transfer. In the thermal equilibrium model, the interfacial heat transfer loss is neglected. The entropy generations caused by other three factors can be calculated separately. The above three entropy generations in each cell are given by:

$$\dot{S}_{gen,f} = \frac{\dot{Q}_f}{T_{f,i}} - \frac{\dot{Q}_f}{T_{f,i+1}} = \frac{\varepsilon k_f A_{reg} \Delta T_{f,i}^2}{T_{f,i} T_{f,i+1} \Delta x} \tag{21}$$

$$\dot{S}_{gen,s} = \frac{\dot{Q}_s}{T_{s,i}} - \frac{\dot{Q}_s}{T_{s,i+1}} = \frac{(1-\varepsilon) k_{s,eff} A_{reg} \Delta T_{s,i}^2}{T_{s,i} T_{s,i+1} \Delta x} \tag{22}$$

$$\dot{S}_{gen,p} = -\dot{m} R \ln\left(\frac{p_{i+1}}{p_i}\right) \tag{23}$$

where $\dot{S}_{gen,f}$, $\dot{S}_{gen,s}$ and $\dot{S}_{gen,p}$ represent entropy generations caused by gas conduction, solid conduction and the pressure drop, respectively. The static temperature and dynamic pressure are area-averaged values for each node, subscript i and $i+1$ represent two adjacent nodes, and Δx is the distance between them. There is no temperature difference between the fluid and solid matrix in the thermal equilibrium model.

Fig. 6 shows the distributions of different entropy generations inside the regenerator. It is observed that, from warm to cold end, the pressure drop loss is dominant during the first about 85% of regenerator length. However, from about 80% of length, the solid conduction loss begins to increase dramatically, which surpasses the pressure drop loss at about 85% of length and becomes dominant. Along the whole regenerator length, $\dot{S}_{gen,p}$ decreases monotonously. The reason is the fluid velocity drops steadily through the porous matrix, and the Darcy and Forchheimer terms are proportional to the velocity and the square velocity, respectively, thereby resulting in less viscous and inertial losses near the cold end. By contrast, $\dot{S}_{gen,f}$ and $\dot{S}_{gen,s}$ share similar changing tendencies, which go up gradually during the first about 60% of length, then increase dramatically, and finally decreases sharply at about 93% of regenerator length, at which both the gas conduction loss or the solid conduction one reaches their respective maximum values. The main reason for the variations of $\dot{S}_{gen,f}$ and $\dot{S}_{gen,s}$ is due to the temperature profiles along the regenerator. Table 5 gives total entropy generations inside the regenerator, in which the pressure drop loss accounts for about 84% of the total.

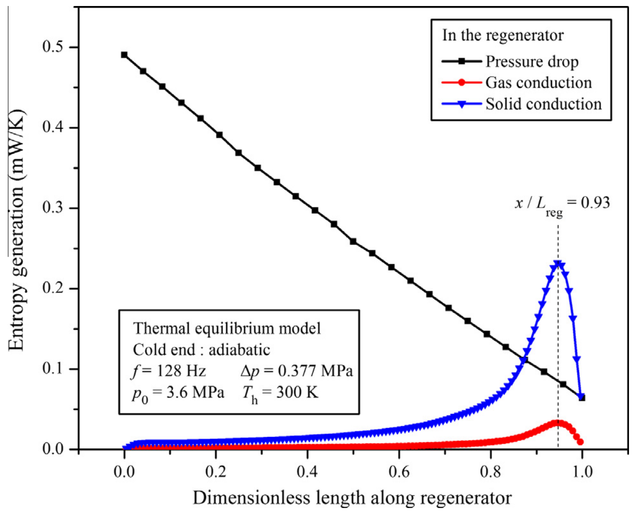

Fig. 6. Distribution of different entropy generations inside the regenerator for Case 1.

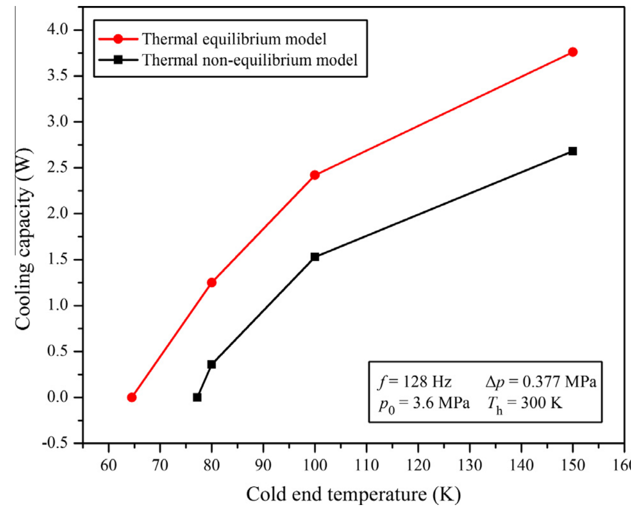

Fig. 7. Comparison of cooling capacities between thermal equilibrium and non-equilibrium models.

Table 5
Total entropy generations inside the regenerator in Case 1.

Terms	Entropy generations (mW/K)
$\dot{S}_{gen,f}$	0.78
$\dot{S}_{gen,s}$	5.24
$\dot{S}_{gen,p}$	30.80

3.2. Non-thermal equilibrium model

In the above simulations, Cases 1–4 are all based on the thermal equilibrium model for porous matrix, in which the heat transfer coefficient between the fluid and solid matrix is assumed to be infinite, thereby the imperfect interfacial heat transfer losses are neglected. In order to provide the more accurate simulations, Case 5 employs the thermal non-equilibrium model. Two different energy conservation equations are calculated for the fluid and solid, respectively. The heat transfer coefficient and interfacial area density for porous zones are given in Table 2.

When the simulation of Case 5 reaches the steady-periodic state, the no-load temperature of the thermal non-equilibrium model increases to about 77 K, about 12.5 K higher than 64.5 K in the thermal equilibrium model. In addition, the amplitude of the temperature variations is about 0.3 K, slightly smaller than 0.5 K in Case 1.

Fig. 7 shows the cooling capacities at 80 K, 100 K and 150 K of cold end temperatures for two different models. A cooling power of 0.36 W at 80 K can be achieved with the thermal non-equilibrium model. The cooling power difference between two models remains about 0.9 W within the simulated temperature range. The irreversible interfacial heat transfer losses in the regenerator, WHX and CHX are responsible for this constant difference.

Fig. 8 shows the temporal variations of the facet averaged temperature of the gas and solid matrix at the midpoint of the regenerator. It shows that the phase of solid temperature variations lags about 0.12π behind the gas, and thus the solid temperature is higher than the gas temperature in half a cycle, whereas the case reverses in the next semi-cycle. In addition, the amplitude of solid temperature variations is about 0.63 K, which is slightly smaller than 0.67 K of the gas. The reason for the difference of 0.04 K is that the stainless steel material has a larger ratio between the thermal capacity and the heat transfer coefficient than the helium.

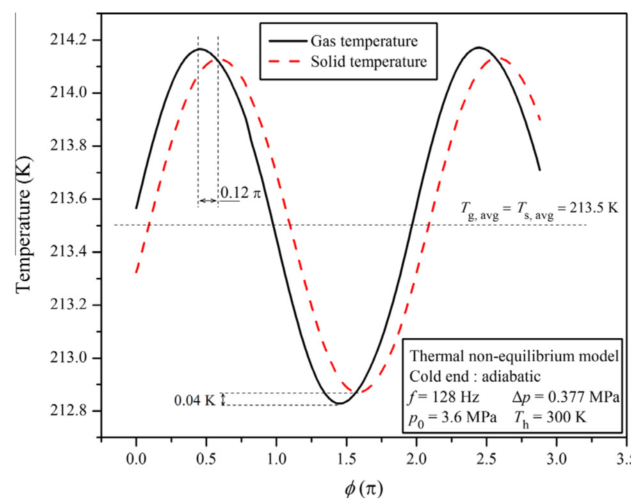

Fig. 8. Variations of the facet averaged temperature at the midpoint of the regenerator for Case 5.

For this thermal non-equilibrium model, the imperfect interfacial heat transfer loss is taken into account. The entropy generation caused by this factor in each cell is given by:

$$\dot{S}_{gen,fs} = \frac{\dot{Q}_{fs}}{T_{f,i}} - \frac{\dot{Q}_{fs}}{T_{s,i}} = \frac{A_{fs}h_{fs}|T_{s,i} - T_{f,i}|^2}{T_{f,i}T_{s,i}} A_{reg}\Delta x \tag{24}$$

The distributions of entropy generations along the regenerator are shown in Fig. 9. It is observed that the pressure drop loss is dominant during the first about 78% of regenerator length, about 7% smaller than 85% of the thermal equilibrium model, while the imperfect interfacial heat transfer loss begins to increase dramatically from about 60% of length, which surpasses the pressure drop loss at about 78% of length and becomes dominant. Compared with the thermal equilibrium model, the solid conduction loss becomes less important due to the separate energy conservation equation for solid matrix. Similar to Case 1, the pressure drop also decreases monotonously from warm to cold end, while $\dot{S}_{gen,fs}$, $\dot{S}_{gen,f}$ and $\dot{S}_{gen,s}$ share similar changing tendencies, which increase steadily during the first about 60% of length, then go up dramatically and reach the maximum values at about 91% of length, very close to 93% in the thermal equilibrium model, and finally decrease sharply near the cold end.

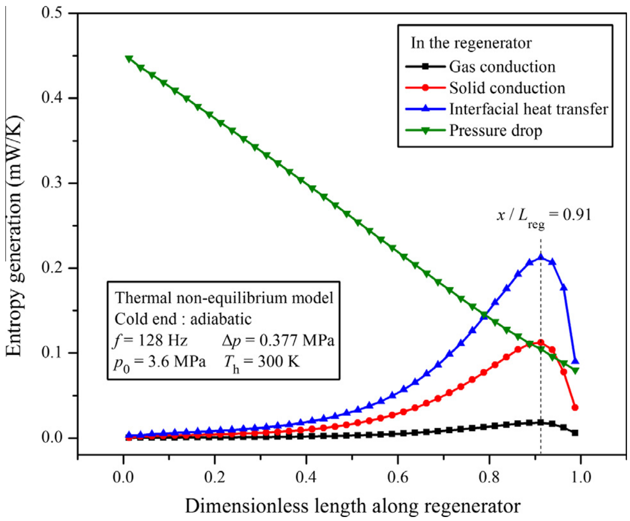

Fig. 9. Distribution of entropy generations along the regenerator for Case 5.

Table 6
Total entropy generations inside the regenerator in Case 5.

Terms	Entropy generations (mW/K)
$\dot{S}_{gen,f}$	0.67
$\dot{S}_{gen,s}$	3.99
$\dot{S}_{gen,fs}$	7.83
$\dot{S}_{gen,p}$	31.03

Table 6 provides total entropy generations caused by all of four factors inside the regenerator for Case 5. Compared with Case 1, conduction terms fall slightly and pressure drop shows little change. The interfacial heat transfer losses are almost twice as large as solid conduction losses, and the pressure drop losses are still dominant, which are 1.5 times larger than the sum of other terms.

The investigation of entropy generations can offer us guidance about optimizing the solid matrix to reduce the regenerator loss. For example, the pressure drop loss can be decreased effectively by using coarser screens near the warm end, and the material with lower heat conductivity and larger specific heat capacity as well can be adopted near the cold end to reduce the solid conduction loss, etc.

5. Conclusions

In order to investigate the physical mechanism and flow characteristics inside a coaxial miniature system at very high frequencies, this paper establishes a two-dimensional axis-symmetric CFD model of a miniature coaxial SPTC weighting about 920 g and operating at 128 Hz. Based on the model, the systematic simulations of performance characteristics are firstly conducted with the thermal equilibrium model, and the results show that the cooling performance is worse than that of 1-D simulation due to the multi-dimensional flow effects. The regenerator losses including gas and solid conduction and the pressure drop are calculated, respectively, and it indicates that the pressure drop loss is dominant during the first about 85% of regenerator length, and it decreases monotonously from warm to cold end due to the steadily decreasing Darcy and Forchheimer terms. The gas and solid conduction losses share similar changing tendencies, and the solid conduction loss begins to increase dramatically from about 80% of length, which surpasses the pressure drop loss at about 85% of length and becomes dominant. The main reason for the variations is the temperature profiles along the regenerator. The investigation of entropy generations can offer us guidance on optimizing the solid matrix to reduce the regenerator loss.

In order to provide the more accurate simulations, the thermal non-equilibrium model is employed for solid matrix. Because of the additional irreversible interfacial heat transfer losses, the no-load temperature increases to about 77 K, and the cooling capacity is down to 0.36 W at 80 K. The pressure drop loss is dominant during the first about 78% of regenerator length, while the imperfect interfacial heat transfer loss increases sharply from about 60% of length and surpasses the pressure drop loss at about 78% of length. Unlike the thermal equilibrium model, the solid conduction loss becomes less important due to the separate energy conservation equation for solid matrix.

Acknowledgements

This work is financially supported by The National Basic Research Program of China (No. 2013CB632802), The Chinese Academy of Sciences (No. XDA04060502) and The Science and Technology Commission of Shanghai Municipality (No. 15521104900).

References

[1] Peterson RB, Al Hazmy M. Size limits for Stirling cycle refrigerators and cryocoolers. Adv Cryog Eng 1998;43:997–1002.
[2] Shire JM, Mujezinovic A, Phelan PE. Investigation of microscale cryocoolers. Cryocoolers 1999;10:663–70.
[3] Radebaugh R, O'Gallagher A. Regenerator operation at very high frequencies for microcryocoolers. Adv Cryog Eng 2006;51:1919–28.
[4] Petach M, Waterman M, Tward E, et al. Pulse tube microcooler for space applications. Cryocoolers 2007;14:89–93.
[5] Petach M, Waterman M, Pruitt G, et al. High frequency coaxial pulse tube microcooler. Cryocoolers 2009;15:97–103.
[6] Nguyen T, Petach M, Michaelian M, et al. Space micro pulse tube cooler. Cryocoolers 2011;16:97–101.
[7] Olson JR, Champagne P, Roth E, et al. Microcryocooler for tactical and space applications. Adv Cryog Eng 2014;59:357–64.
[8] Vanapalli S, Lewis M, Grossman G, et al. Modeling and experiments on fast cooldown of a 120 Hz pulse tube cryocooler. Adv Cryog Eng 2008;53:1429–36.
[9] Radebaugh R, Garaway I, Veprik AM. Development of miniature, high frequency pulse tube cryocoolers. In: Proceedings of SPIE 7660; 2010.
[10] Lopes D, Duval JM, Charles I, et al. Design and characterization of very high frequency pulse tube prototypes. Adv Cryog Eng 2012;57:1487–94.
[11] Ju YL, Wang C, Zhou Y. Numerical simulation and experimental verification of the oscillating flow in pulse tube refrigerator. Cryogenics 1998;38:169–76.
[12] Flake B, Razani A. Modeling pulse tube cryocoolers with CFD. Adv Cryog Eng 2004;49:1493–9.
[13] Cha JS, Ghiaasiaan SM, Desai PV, et al. Multi-dimensional flow effects in pulse tube refrigerators. Cryogenics 2006;46:658–65.
[14] Ashwin TR, Narasimham GSVL, Jacob S. CFD analysis of high frequency miniature pulse tube refrigerators for space applications with thermal non-equilibrium model. Appl Therm Eng 2010;30:152–66.
[15] Fluent 6.3 User's Guide. Fluent Inc. http://www.fluentusers.com.
[16] Dang HZ. High-capacity 60 K single-stage coaxial pulse tube cryocoolers. Cryogenics 2012;52:205–11.
[17] Dang HZ. Development of high performance moving-coil linear compressors for space Stirling-type pulse tube cryocoolers. Cryogenics 2015;68:1–18.
[18] Robbert A. Cryogenic regenerative heat exchangers. New York: Plenum Press; 1997. p. 48–54.
[19] Macdonald IF, El-sayed MS, Mow K, et al. Flow through porous media – the Ergun equation revisited. Int Eng Chem Fundament 1979;18:199–208.
[20] Lewis M, Radebaugh R. Measurement of heat conduction through metal spheres. Cryocoolers 2001;11:419–25.
[21] Gedeon D. Baseline Stirling modeling. Athens (OH): Gedeon Associates; 1999.